Metalenses at visible wavelengths: Diffraction-limited focusing and subwavelength resolution imaging

The Harvard community has made this article openly available. Please share how this access benefits you. Your story matters

Citation	Khorasaninejad, Mohammadreza, Wei Ting Chen, Robert C. Devlin, Jaewon Oh, Alexander Y. Zhu, and Federico Capasso. 2016. "Metalenses at Visible Wavelengths: Diffraction-Limited Focusing and Subwavelength Resolution Imaging." Science 352 (6290): 1190–94. https://doi.org/10.1126/science.aaf6644.
Citable link	http://nrs.harvard.edu/urn-3:HUL.InstRepos:41371607
Terms of Use	This article was downloaded from Harvard University's DASH repository, WARNING: This file should NOT have been available for downloading from Harvard University's DASH repository.

RESEARCH ARTICLE

APPLIED OPTICS

Metalenses at visible wavelengths: Diffraction-limited focusing and subwavelength resolution imaging

Mohammadreza Khorasaninejad,[1]* Wei Ting Chen,[1]* Robert C. Devlin,[1]* Jaewon Oh,[1,2] Alexander Y. Zhu,[1] Federico Capasso[1]†

Subwavelength resolution imaging requires high numerical aperture (NA) lenses, which are bulky and expensive. Metasurfaces allow the miniaturization of conventional refractive optics into planar structures. We show that high-aspect-ratio titanium dioxide metasurfaces can be fabricated and designed as metalenses with NA = 0.8. Diffraction-limited focusing is demonstrated at wavelengths of 405, 532, and 660 nm with corresponding efficiencies of 86, 73, and 66%. The metalenses can resolve nanoscale features separated by subwavelength distances and provide magnification as high as 170×, with image qualities comparable to a state-of-the-art commercial objective. Our results firmly establish that metalenses can have widespread applications in laser-based microscopy, imaging, and spectroscopy.

Metasurfaces are composed of subwavelength-spaced phase shifters at an interface, which allows for unprecedented control over the properties of light (1, 2), and have advanced optical technology by enabling versatile functionalities in a planar structure (1–30). Various optical components, ranging from lenses, holograms and gratings to polarization-selective devices, have been demonstrated using silicon-based (7–19) and plasmonic metasurfaces (3, 4, 21–27). However, the high intrinsic losses of silicon and plasmonic materials in the visible range (400 to 700 nm) have prevented the realization of highly efficient metasurfaces in this region. Although this challenge can be partially overcome by using dielectric materials with a transparency window in the visible spectrum (e.g., GaP, SiN, and TiO_2), achieving full control over the phase of light requires precise, high-aspect-ratio nanostructures, which are in turn restricted by available nanofabrication methods. Recently, we have developed an approach based on titanium dioxide (TiO_2) (31) prepared by atomic layer deposition (ALD) (32), which enables fabrication of high-aspect-ratio metasurfaces that are lossless in the visible spectrum. Here, we demonstrate highly efficient metalenses at visible wavelengths (λ = 405, 532, and 660 nm) with efficiencies as high as 86%. They have high numerical apertures (NA) of 0.8 and are capable of focusing light into diffraction-limited spots. At their respective design wavelengths, these focal spots are smaller by a factor of ~1.5 than those from a commercially available, high-NA objective (100× Nikon CFI 60; NA = 0.8). Imaging using these metalenses shows that they can yield subwavelength resolution, with image qualities comparable to that obtained by the commercial objective.

Planar lens design and fabrication

Typical high-NA objectives consist of precision-engineered compound lenses which make them bulky and expensive, limiting their applications and hindering their integration into compact and cost-effective systems. Singlet planar lenses with high NA in the visible range are in particularly high demand due to their potential widespread applications in imaging, microscopy, and spectroscopy. Although visible planar lenses can be realized by diffractive components, high NA and efficiency are not attainable because their constituent structures are of wavelength scale, which precludes an accurate phase profile.

Figure 1A shows a schematic of a transmissive dielectric metalens. The building blocks of the metalens are high-aspect-ratio TiO_2 nanofins (Fig. 1, B to E). To function like a spherical lens, the phase profile $\varphi_{nf}(x, y)$ of the metalens needs to follow (25)

$$\varphi_{nf}(x, y) = \frac{2\pi}{\lambda_d}\left(f - \sqrt{x^2 + y^2 + f^2}\right) \quad (1)$$

where λ_d is the design wavelength, x and y are the coordinates of each nanofin, and f is the focal length. This phase profile is imparted via rotation of each nanofin at a given coordinate (x, y) by an angle $\theta_{nf}(x, y)$ (Fig. 1E). In the case of right-handed circularly polarized incident light, these rotations yield a phase shift, $\varphi_{nf}(x, y) = 2\theta_{nf}(x, y)$,

accompanied by polarization conversion to left-handed circularly polarized light (33, 34). Thus, each nanofin at (x, y) is rotated by an angle

$$\theta_{nf}(x, y) = \frac{\pi}{\lambda_d}\left(f - \sqrt{x^2 + y^2 + f^2}\right) \quad (2)$$

To maximize the polarization conversion efficiency, the nanofins should operate as half-waveplates (11–13, 21). This is achieved due to the birefringence arising from the asymmetric cross section of nanofins with appropriately designed height, width, and length (Fig. 1, C and D). Simulations using a commercial finite difference time domain (FDTD) solver (Lumerical Inc., Vancouver) in Fig. 1F show that conversion efficiencies as high as 95% are achieved and that the metalens can be designed for a desired wavelength via tuning of nanofin parameters. The conversion efficiency is calculated as the ratio of transmitted optical power with opposite helicity to the total incident power.

Three distinct metalenses were fabricated with respective design wavelengths (λ_d) of 660, 532, and 405 nm. All of these metalenses have the same diameter of 240 μm and a focal length of 90 μm, yielding a NA = 0.8. The fabrication process uses electron-beam lithography to create the lens pattern in the resist (ZEP 520A). The thickness of the resist is the same as the designed nanofin height, H, and ALD is subsequently used to deposit amorphous TiO_2 onto the developed resist. Amorphous TiO_2 is chosen because it has low surface roughness, no absorption at visible wavelengths, and a sufficiently high refractive index (~2.4). Due to the ALD process being conformal, a deposition thickness of at least $W/2$ (where W is the nanofin width) is required to produce void-free nanofins (31). However, the deposition also leaves a TiO_2 film of equal thickness on top of the resist, which is then removed by controlled blanket reactive ion etching. Finally, the remaining electron beam resist is stripped, and only high-aspect-ratio nanofins remain. Figure 1, G and H, shows optical and scanning electron microscope (SEM) images of a fabricated metalens, respectively. Additional SEM micrographs of the metalens are shown in fig. S1 (35). Because the geometrical parameters of the nanofins are defined by the resist rather than top-down etching, high-aspect-ratio nanofins with ~90° vertical sidewalls are obtained. It is important to note that achieving these atomically smooth sidewalls is very challenging with a conventional top-down approach (e.g., lithography followed by dry etching), because inevitable lateral etching results in surface roughness and tapered/conical nanostructures.

Characterizing metalens performance

The metalenses' focal spot profiles and efficiencies were measured using the experimental setup shown in fig. S2. Figure 2A shows a highly symmetric focal spot that is obtained for the metalens at its design wavelength λ_d = 660 nm. The vertical cut of the focal spot is also shown in Fig. 2G with a diffraction-limited $\left(\frac{\lambda}{2 \times NA}\right)$ full-width at half-maximum (FWHM) of 450 nm. Figure 2, B and H, show the focal spot of the metalens

[1]Harvard John A. Paulson School of Engineering and Applied Sciences, Harvard University, Cambridge, MA 02138, USA. [2]University of Waterloo, Waterloo, ON N2L 3G1, Canada. *These authors contributed equally to this work. †Corresponding author. Email: capasso@seas.harvard.edu
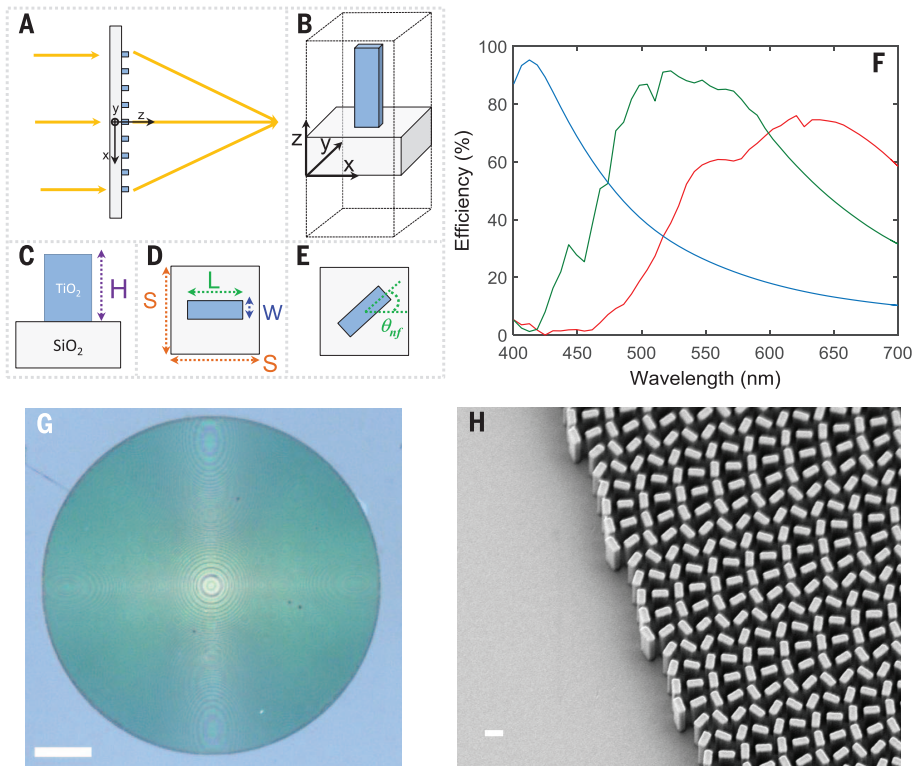
Fig. 1. Design and fabrication of metalenses. (**A**) Schematic of the metalens and its building block, the TiO$_2$ nanofin. (**B**) The metalens consists of TiO$_2$ nanofins on a glass substrate. (**C** and **D**) Side and top views of the unit cell showing height H, width W, and length L of the nanofin, with unit cell dimensions $S \times S$. (**E**) The required phase is imparted by rotation of the nanofin by an angle θ_{nf}, according to the geometric Pancharatnam-Berry phase. (**F**) Simulated polarization conversion efficiency as a function of wavelength. This efficiency is defined as the fraction of the incident circularly polarized optical power that is converted to transmitted optical power with opposite helicity. For these simulations, periodic boundary conditions are applied at the x and y boundaries and perfectly matched layers at the z boundaries. For the metalens designed at λ_d = 660 nm (red curve), nanofins have W = 85, L = 410, and H = 600 nm, with center-to-center spacing S = 430 nm. For the metalens designed at λ_d = 532 nm (green curve), nanofins have W = 95, L = 250, and H = 600 nm, with center-to-center spacing S = 325 nm. For the metalens designed at λ_d = 405 nm (blue curve), nanofins have W = 40, L = 150, and H = 600 nm, with center-to-center spacing S = 200 nm. (**G**) Optical image of the metalens designed at the wavelength of 660 nm. Scale bar, 40 μm. (**H**) SEM micrograph of the fabricated metalens. Scale bar, 300 nm.

designed at the wavelength of 532 nm and its corresponding vertical cut. Moreover, this metalens design can be extended to the shorter wavelength region of the visible range, which is of great interest in many areas of optics, such as lithography and photoluminescence spectroscopy. Figure 2C depicts the intensity profile of the focal spot from the metalens designed at the wavelength λ_d = 405 nm with a FWHM of 280 nm (Fig. 2I). Although this wavelength is very close to the band gap of TiO$_2$ λ_g = 360 nm, the absorption loss is still negligible (*31*).

To compare the performance of our metalenses with a commercially available lens, we selected a state-of-the-art Nikon objective. This objective has the same NA as our metalenses (0.8) and is designed for visible light. Focal spot intensity profiles of the objective at wavelengths of 660, 532, and 405 nm were measured using the same setup as in fig. S2 (see Fig. 2, D to F). A comparison of the corresponding focal spot cross sections in Fig. 2, G to I, and Fig. 2, J to L, reveals

that the metalenses provide smaller (~1.5 times) and more symmetric focal spots. This can be understood because conventional high-NA objectives are designed to image under broadband illumination. That is, wavefront aberrations need to be corrected for multiple wavelengths over a range of angles of incidence to meet industry standards for the required field of view. This is typically implemented by cascading a series of precisely aligned compound lenses. Fabrication imperfections in each individual optical lens and residual aberration errors, particularly spherical aberration, result in a focal spot size larger than theoretical predictions (*36*). In contrast, our metalens is designed to have a phase profile free of spherical aberration for normally incident light, which results in a diffraction-limited spot at a specific design wavelength (*37*). For example, the theoretical root mean squares of the wave aberration function (WAF$_{RMS}$) for the metalenses designed for 405, 532, and 660 nm are 0.049λ, 0.060λ and 0.064λ, respectively. These values are

very close to the condition for a perfect spherical wavefront (*37*). We also calculated the Strehl ratio from the measured beam profiles for the three metalenses at their design wavelengths and found that they are close to 0.8 (see materials and methods and fig. S3), consistent with the observed diffraction-limited focusing. In addition, due to the use of the geometric phase, the phase profile of the metalens is only dependent on the rotation of the nanofins. This is controlled with very high precision, as is characteristic of electron-beam lithography. Alternatively, other high-throughput lithography methods such as deep-ultraviolet (UV) can provide similar fabrication accuracy.

It is important to note that although the metalenses were designed at specific wavelengths, we still observe wavelength-scale focal spots at wavelengths away from the design. For example, for the metalens designed at λ_d = 532 nm, we measured focal spot sizes of 720 and 590 nm at wavelengths of λ = 660 and 405 nm, respectively (fig. S4). The broadening of the focal spots with respect to the theoretical diffraction-limited values comes from chromatic aberration because metasurfaces are inherently dispersive. Chromatic aberrations in our metalens are more pronounced than the lenses based on refractive optics, resulting in a wavelength-dependent focal length (fig. S5A). This is generally not an issue for laser-related imaging, microscopy, and spectroscopy because monochromatic sources with narrow linewidths are used. For example, in Raman microscopes/spectrometers, a 532-nm laser with a linewidth of a few picometers is common. In this case, the linewidth-induced broadening of the focal spot size and change in focal length is negligible.

We also measured the focusing efficiency of the metalenses. As shown in Fig. 3A, the metalens designed at λ_d = 660 nm has a focusing efficiency of 66%, which remains above 50% in most of the visible range. Figure 3A also shows the measured focusing efficiency of the metalens designed at λ_d = 532 nm. This metalens has a focusing efficiency of 73% at its design wavelength. In addition, we measured the beam intensity profile of this metalens in the x-z cross section within a 40-μm span around the focal point (Fig. 3B). Details of this measurement are discussed in the supplementary materials (*35*) (see fig. S2 and materials and methods). The negligible background signal not only demonstrates excellent phase realization, where the beam converges to a diffraction-limited spot, but also shows the high conversion efficiency of each nanofin. For the metalens designed at the wavelength of 405 nm, a measured focusing efficiency of 86% is achieved. The latter measurement was done using a diode laser (Ondax Inc., Monrovia, CA) because the shortest wavelength that our tunable laser (SuperK Varia) can provide was ~470 nm. All of the efficiency measurements were performed using right circularly polarized incident light. However, the polarization sensitivity of the design can be overcome by implementing the phase profile using circular cross section nanopillars in
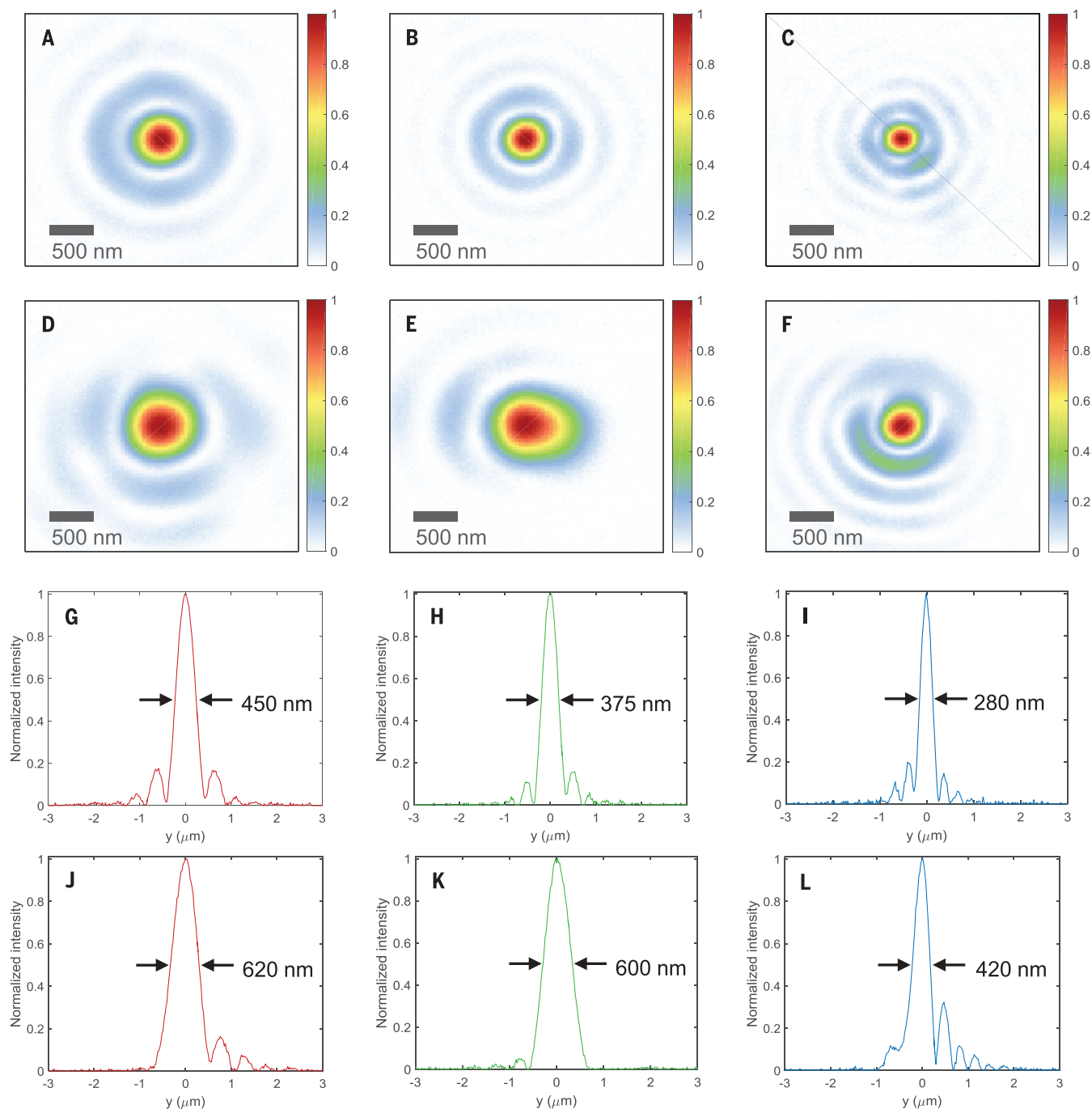
Fig. 2. Diffraction-limited focal spots of three metalenses (NA = 0.8) and comparison with a commercial state-of-the-art objective. (**A** to **C**) Measured focal spot intensity profile of the metalens designed at (**A**) λ_d = 660, (**B**) λ_d = 532, and (**C**) λ_d = 405 nm. (**D** to **F**) Measured focal spot intensity profiles of the objective (100× Nikon CFI 60, NA = 0.8) at wavelengths of (**D**) 660, (**E**) 532, and (**F**) 405 nm. (**G** to **I**) Corresponding vertical cuts of the metalenses' focal spots. Metalenses designed at wavelengths of 660,

532, and 405 nm have FWHMs = 450, 375, and 280 nm, respectively. The symmetric beam profiles and diffraction-limited focal spot sizes are related to the quality of the fabricated metalenses and accuracy of the phase realization. (**J** to **L**) Corresponding vertical cuts of the focal spots of the objective, at wavelengths of (**J**) 660, (**K**) 532, and (**L**) 405 nm. FWHMs of the focal spots are labeled on the plots. These values are ~1.5 times as large as those measured for the metalenses.

which the phase is controlled via changing their diameters.

Imaging demonstration

To demonstrate the use of our metalens for practical imaging, we fabricated a metalens with diameter D = 2 mm and focal length f = 0.725 mm giving NA = 0.8. First, we characterized the imaging resolution using the 1951 United States Air Force (USAF) resolution test chart (Thorlabs Inc., Jessup, MD) as the target object. The measurement configuration is shown in fig. S6. Figure 4A

shows the image formed by the metalens. The light source was a tunable laser (SuperK Varia) set at 530 nm with a bandwidth of 5 nm. Because the resulting image was larger than our charge-coupled device (CCD) camera, we projected the image onto a translucent screen and took its

photo with a Canon digital single-lens reflex (DSLR) camera. The smallest features in this object are lines with widths of 2.2 μm and center-to-center distances of 4.4 μm (the bottom element in the highlighted region). A similar image quality is achieved at wavelengths covering the visible spectrum (fig. S7). Images of the smallest features were taken with a CCD camera shown in Fig. 4, B to E, at wavelengths of 480, 530, 590, and 620 nm, respectively. It is clear that the metalens can resolve these micrometer-sized lines. We repeated a similar experiment using a Siemens star target and showed that all features can be resolved over the whole visible range (figs. S8 and S9). As mentioned previously, the focal length of the metalens varies as the wavelength changes, resulting in different levels of magnification (fig. S5B). In our experimental setup, we used the metalens together with a tube lens (f = 100 mm), giving a magnification of 138× (100/0.725) at 530 nm. For wavelengths of 480, 590, and 620 nm, magnifications of 124×, 152×, and 167× are obtained, respectively, by comparing the ratio of the image sizes formed on the camera to the known physical size of the USAF test object.

To characterize the effects of chromatic aberration, we imaged the same object at 530 nm without changing the distance between the metalens and the object, while varying the bandwidth of the source from 10 to 100 nm (the limit of our tunable laser). These results are shown in Fig. 4, F to I. Although the quality of the image slightly degrades from increasing the bandwidth, the smallest features are still resolvable even at the maximum bandwidth of 100 nm. Finally, for comparison of the imaging quality to that of a conventional objective, we fabricated an H-shaped object composed of arrays of holes with gaps of ~800 nm using a focused ion beam (FIB). An SEM micrograph of the object is shown in Fig. 4J. The image formed by the metalens (Fig. 4K) has comparable quality to the one formed by the 100× Nikon objective (Fig. 4L) with the same NA = 0.8. The change in the image sizes comes from the difference in the magnification of the imaging systems. We also tested the resolution limit of our metalens: Four holes with subwavelength gap sizes of ~450 nm can be well resolved (Fig. 4M). This value agrees with the measured modulation transfer function of our metalens (supplementary materials and fig. S10).

Concluding remarks

The demonstrated visible-range metalenses, using TiO$_2$ with NA = 0.8 and efficiencies as high as 86%, show that they are able to provide diffraction-limited focal spots at arbitrary design wavelengths, which make them ideal devices for use in optical lithography, laser-based microscopy, and spectroscopy. Providing a magnification as high as 170× and capable of resolving structures with subwavelength spacing, the compact configuration of our metalenses can enable portable/handheld instruments for many applications. Although our metalenses are subject to chromatic aberrations, the latter can be corrected with approaches such as dispersive phase compensation demonstrated
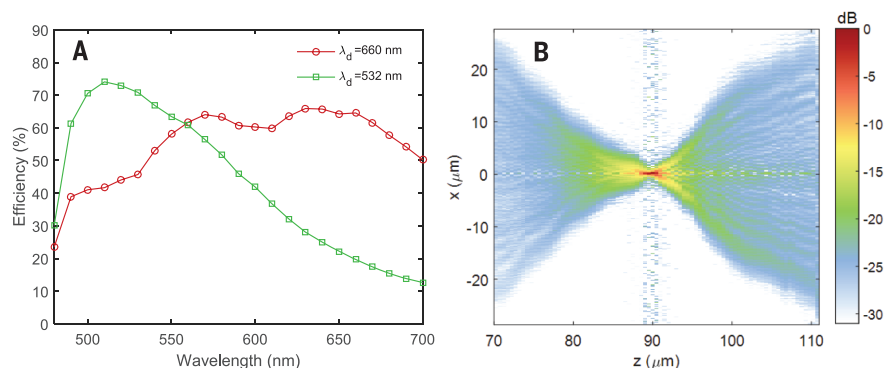

Fig. 3. Characterization of the metalenses. (A) Measured focusing efficiency of the metalenses designed at wavelengths of 660 nm and 532 nm. (B) Intensity distribution in dB of the x-z plane, showing the evolution of the beam from 20 μm before and 20 μm after the focus. This measurement was performed on the metalens designed at λ$_d$ = 532 nm. The wavelength of incident light was 532 nm.
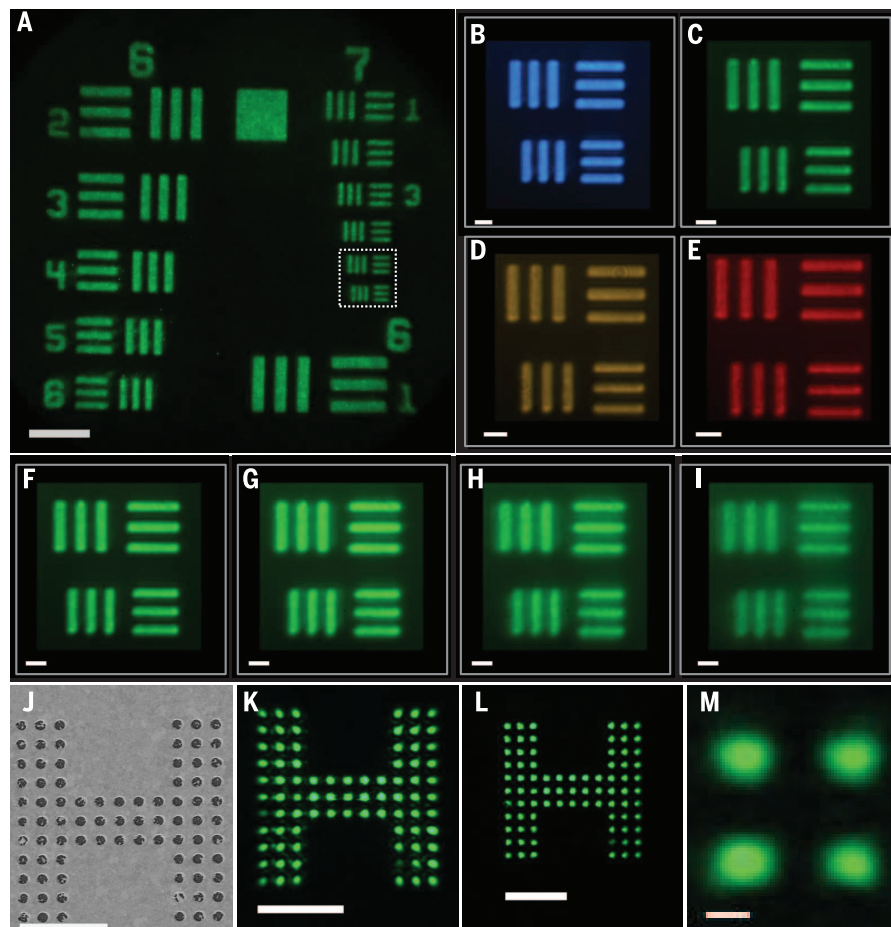

Fig. 4. Imaging with a metalens designed at λ$_d$ = 532 nm with diameter D = 2 mm and focal length f = 0.725 mm. (A) Image of 1951 USAF resolution test chart formed by the metalens taken with a DSLR camera. Laser wavelength is set at 530 nm. Scale bar, 40 μm. (B to E) Images of the highlighted region in Fig. 4A at wavelengths of (B) 480, (C) 530, (D) 590, and (E) 620 nm. Scale bar, 5 μm. (F to I) Images of the highlighted region in Fig. 4A at a center wavelength of 530 nm and with different bandwidths: (F) 10, (G) 30, (H) 50, and (I) 100 nm. Scale bar, 5 μm. (J) Nanoscale target prepared by FIB. The smallest gap between neighboring holes is ~800 nm. (K) Image of target object (Fig. 4J) formed by the metalens. (L) Image of target object formed by the commercial state-of-the-art objective. Scale bar, 10 μm in Fig. 4, J to L. (M) Image formed by the metalens shows that holes with subwavelength gaps of ~450 nm can be resolved. Scale bar, 500 nm.

in (9, 10). The single-layer lithographic fabrication of the metalenses can make use of existing foundry technology (deep-UV steppers) used in the manufacturing of integrated circuits, which is crucial for high throughput.

REFERENCES AND NOTES

1. N. Yu, F. Capasso, *Nat. Mater.* **13**, 139–150 (2014).
2. A. V. Kildishev, A. Boltasseva, V. M. Shalaev, *Science* **339**, 1232009 (2013).
3. N. Yu et al., *Science* **334**, 333–337 (2011).
4. X. Ni, N. K. Emani, A. V. Kildishev, A. Boltasseva, V. M. Shalaev, *Science* **335**, 427–427 (2012).
5. A. Silva et al., *Science* **343**, 160–163 (2014).
6. F. Monticone, N. M. Estakhri, A. Alù, *Phys. Rev. Lett.* **110**, 203903 (2013).
7. S. Jahani, Z. Jacob, *Nat. Nanotechnol.* **11**, 23–36 (2016).
8. D. Fattal, J. Li, Z. Peng, M. Fiorentino, R. G. Beausoleil, *Nat. Photonics* **4**, 466–470 (2010).
9. F. Aieta, M. A. Kats, P. Genevet, F. Capasso, *Science* **347**, 1342–1345 (2015).
10. M. Khorasaninejad et al., *Nano Lett.* **15**, 5358–5362 (2015).
11. D. Lin, P. Fan, E. Hasman, M. L. Brongersma, *Science* **345**, 298–302 (2014).
12. Z. Bomzon, G. Biener, V. Kleiner, E. Hasman, *Opt. Lett.* **27**, 285–287 (2002).
13. M. Khorasaninejad, K. B. Crozier, *Nat. Commun.* **5**, 5386 (2014).
14. K. E. Chong et al., *Nano Lett.* **15**, 5369–5374 (2015).
15. A. Arbabi, Y. Horie, A. J. Ball, M. Bagheri, A. Faraon, *Nat. Commun.* **6**, 7069 (2015).
16. C. J. Chang-Hasnain, *Semicond. Sci. Technol.* **26**, 014043 (2011).
17. Y. Yang et al., *Nano Lett.* **14**, 1394–1399 (2014).
18. M. Khorasaninejad, W. Zhu, K. Crozier, *Optica* **2**, 376–382 (2015).
19. P. Spinelli, M. A. Verschuuren, A. Polman, *Nat. Commun.* **3**, 692 (2012).
20. S. Liu et al., *Optica* **1**, 250–256 (2014).
21. G. Zheng et al., *Nat. Nanotechnol.* **10**, 308–312 (2015).
22. E. T. Rogers et al., *Nat. Mater.* **11**, 432–435 (2012).
23. S. Sun et al., *Nano Lett.* **12**, 6223–6229 (2012).
24. S. Larouche, Y.-J. Tsai, T. Tyler, N. M. Jokerst, D. R. Smith, *Nat. Mater.* **11**, 450–454 (2012).
25. F. Aieta et al., *Nano Lett.* **12**, 4932–4936 (2012).
26. X. Yin, Z. Ye, J. Rho, Y. Wang, X. Zhang, *Science* **339**, 1405–1407 (2013).
27. W. T. Chen et al., *Nano Lett.* **14**, 225–230 (2014).
28. A. Grbic, L. Jiang, R. Merlin, *Science* **320**, 511–513 (2008).
29. M. Khorasaninejad, F. Capasso, *Nano Lett.* **15**, 6709–6715 (2015).
30. N. Yu et al., *Science* **317**, 927–929 (2007).
31. R. C. Devlin, M. Khorasaninejad, W.-T. Chen, J. Oh, F. Capasso, arXiv:1603.02735 (2016).
32. A. A. High et al., *Nature* **522**, 192–196 (2015).
33. M. V. Berry, *J. Mod. Opt.* **34**, 1401–1407 (1987).
34. S. Pancharatnam, *Proceedings of the Indian Academy of Sciences, Section A* (Springer, 1956), vol. 44, pp. 398–417.
35. Supplementary materials are available on *Science* Online.
36. M. Yoshida, U.S. Patent App. 13/760,681, 2013.
37. F. Aieta, P. Genevet, M. Kats, F. Capasso, *Opt. Express* **21**, 31530–31539 (2013).

REPORTS

WATER CHEMISTRY

Structure and torsional dynamics of the water octamer from THz laser spectroscopy near 215 μm

William T. S. Cole,[1]* James D. Farrell,[2]* David J. Wales,[2]† Richard J. Saykally[1]†

Clusters of eight water molecules play an important role in theoretical analysis of aqueous structure and dynamics but have proven to be challenging experimental targets. Here we report the high-resolution spectroscopic characterization of the water octamer. Terahertz (THz) vibration-rotation-tunneling (VRT) spectroscopy resolved 99 transitions with 1 part per million precision in a narrow range near 46.5 wave numbers, which were assigned to the h_{16} octamer via detailed isotope dilution experiments. Fitting to a semi-rigid symmetric top model supports predictions of two coexisting cuboidal structures and provides precise values for the changes in their rotational constants. Comparison with theory and previous spectroscopic data provides a characterization of the two structures and the observed torsional vibration and supports the prediction that the D_{2d} symmetry structure is lower in energy than the S_4 isomer.

Spectroscopic study of water clusters provides accurate benchmarks for detailed characterization of the complex pairwise and many-body forces that operate in bulk water phases, which have proven difficult to adequately capture through bulk experiments or theory (1–4). The need to accomplish this goal is underscored by recurring controversies surrounding the fundamental intermolecular structure and dynamics of water (2, 5, 6). Clusters ranging from dimer through heptamer, as well as nonamer and decamer (7), have been studied in detail by high-precision microwave and terahertz spectroscopy, but the octamer has proven elusive (1, 2, 8–10). Whereas the most stable structures of smaller clusters evolve with size from quasiplanar rings to three-dimensional (3D) cages, the octamer represents the transition to cuboidal (8) structures formed by stacking quasiplanar four- and five-membered rings, a dominant motif in larger systems.

Accordingly, the water octamer has become a benchmark for theory, starting with the early work of Stillinger and David (11), Brink and Glasser (12), and Tsai and Jordan (13). Many groups have since investigated the structures, melting transitions, and hydrogen bond (HB) rearrangement dynamics of the octamer cluster (14–30). However, experimental characterization has been very challenging, with only a few successful mid-infrared (IR) spectroscopy (31–34) and crystallographic studies (35–37). The mid-IR results are particularly interesting, revealing two nonpolar low-energy struc-

tures (Fig. 1) formed by stacking of homodromic tetramer rings with the in-plane HBs directed in either the same (S_4 symmetry) or opposite (D_{2d} symmetry) senses. Both structures possess two distinct monomer environments: single HB donor and double HB donor, with the latter responsible for the association between the two tetramer rings. These structures have subsequently been refined by theory, with several groups calculating the ground state energy difference between the S_4 and the D_{2d} structures to be <0.1 kJ/mol (14–17, 37). Given such a small energy difference, both structures should be present even in very low temperature environments, e.g., supersonic beams.

Here we present the results of a study of the water h_{16}-octamer by terahertz vibration-rotation-tunneling (VRT) spectroscopy, involving the measurement of a very low frequency torsional vibration in both low-lying isomers. Nearly 100 individual vibration-rotation transitions have been measured to parts per million (ppm) accuracy and fitted to a standard semi-rigid symmetric rotor model, producing rotational constants, which, when combined with theoretical values, characterize the structures and vibrational distortions of the cluster. The results are in good agreement with recent theoretical predictions of the HB rearrangement tunneling rates (8) and cluster structures.

In an earlier study, Richardson et al. presented VRT spectra comprising 99 weak transitions measured near 1.4 THz and assigned to the h_{16}-water octamer cluster on the basis of detailed isotopic dilution studies (8). Spectral assignment was not possible at that time. In the same study, application of the ring polymer perturbative instanton method predicted the HB rearrangement tunneling rates for the h_{16}-octamer. Those results indicated that even for the most energetically accessible rearrangement, the magnitude of the tunneling

[1]Department of Chemistry, University of California, Berkeley, CA 94705, USA. [2]Department of Chemistry, University of Cambridge, Cambridge CB2 1EW, UK.
*These authors contributed equally to this work. †Corresponding author. Email: saykally@berkeley.edu (R.J.S.); dw34@cam.ac.uk (D.J.W.)

Editor's Summary

Multifunction planar optics

Specially designed two-dimensional (2D) arrays of nanometer-scale metallic antennas, or metasurfaces, may allow bulky optical components to be shrunk down to a planar device structure. Khorasaninejad *et al.* show that arrays of nanoscale fins of TiO can function as high-end optical lenses. At just a fraction of the size of optical objectives, such planar devices could turn your phone camera or your contact lens into a compound microscope. Maguid *et al.* interleaved sparse 2D arrays of metal antennas to get multifunctional behavior from the one planar device structure (see the Perspective by Litchinitser). The enhanced functionality of such designed metasurfaces could be used in sensing applications or to increase the communication capacity of nanophotonic networks.

Science, this issue pp. 1190 and 1202; see also p. 1177

Article Tools	Visit the online version of this article to access the personalization and article tools: http://science.sciencemag.org/content/352/6290/1190
Permissions	Obtain information about reproducing this article: http://www.sciencemag.org/about/permissions.dtl